Molecular-Level Design of Heterogeneous Chiral Catalysts

Wilfred T. Tysoe, Andrew Gellman, Charles Sykes and Francisco Zaera
Department of Chemistry and Biochemistry, University of Wisconsin-Milwaukee
Department of Chemical Engineering, Carnegie Mellon University
Department of Chemistry, Tufts University
Department of Chemistry, University of California-Riverside

2. What was accomplished under these goals?

For convenience, the accomplishments are discussed under the following categories: naturally chiral surfaces, chirally templated surfaces, one-to-one interactions and catalytic reaction studies.

2.1 Naturally Chiral Surfaces

Conglomerate versus racemate formation on surfaces

It is well documented that crystallization in 3D of racemic mixtures of enantiomers results primarily (in 90% of cases) in the formation of racemate crystals that contain equal numbers of enantiomers in their crystalline unit cells. Physical mixtures of enantiomerically pure crystals (conglomerates) are found only in 10% of cases. In contrast, it has been speculated, and argued on the basis of symmetry that, in 2D adsorbed monolayers one should find preferential conglomerate formation (enantiomerically pure 2D ordered domains). The core argument is that 2D monolayers cannot have inversion symmetry, a common symmetry element in the structures of 3D racemate crystals. The 2D hypothesis is consistent with a number of measurements of equilibrium adsorption of amino acid mixtures made in the course of this DOE grant, but had not been tested rigorously. Gellman has tested the 2D hypothesis by reviewing the literature reporting scanning tunneling microscopy (STM) images of 2D monolayers of chiral adsorbates prepared as racemic mixtures. This work examined the images reported in ~170 papers describing studies of ~150 different adsorbate-substrate systems. Where possible, the 2D monolayer images were identified as either racemates (heterochiral) or conglomerates (homochiral). The net finding of this work, published in *Chemical Society Reviews* is that there is *no preference* for the formation of either type of overlayer in 2D adsorbed monolayers of racemic mixtures.

Enantiospecific adsorption and decomposition of D- and L-Asp mixtures on Cu(643)$^{R\&S}$

Gellman has compared the equilibrium adsorption behaviour of mixtures of *D*- and *L*-Asp on several Cu single crystal surfaces (Figure 1). Here, using enantiospecific isotopic labelling and surface-sensitive techniques, we show that when the two enantiomers of chiral aspartic acid (Asp) are adsorbed on the naturally chiral Cu(643)$^{R\&S}$ surfaces, they decompose enantiospecifically depending on the chirality of the surface. The non-linear kinetics of the surface decomposition mechanism amplifies the difference between the decomposition rate constants of the two adsorbed enantiomers resulting in highly enantiospecific decomposition rates. Furthermore, Gellman also demonstrated that Asp enantiomers aggregate homochirally (as conglomerates) on several chiral and achiral surfaces, amplifying the enantiomeric excess on the surface with respect to that in the gas phase, $|ee_s| > |ee_g|$. Gellman's results show that it is possible to discern the enantiospecific behavior of a complex adsorbate such as Asp and shed light on molecular-level interactions

between enantiomers on surfaces. The enantiospecific isotope labelling methods discussed in this work allow probing of both the qualitative features of the Asp decomposition mechanism on Cu(643)$^{R\&S}$ and quantitative aspects of the adsorption equilibria of enantiomer mixtures.

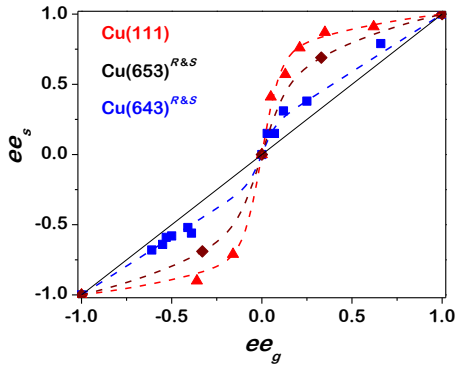

Figure 1: Experimental and fit isotherms for enantiospecific adsorption of Asp/Cu(111) (red), Asp/Cu(653)$^{R\&S}$ (black) and Asp/Cu(643)$^{R\&S}$ (blue). All three exhibit homochiral enantiomer aggregation by amplification of enantiomer excess, $|ee_s| > |ee_g|$. However, there is no sign of enantiospecific adsorption, $ee_s = 0$ at $ee_g = 0$, on the chiral surfaces.

Steady-state catalytic decomposition of aspartic acid on Cu(111)

Gellman has found that the decomposition of aspartic acid (Asp, $HO_2CCH(NH_2)CH_2CO_2H$) to CO_2, $N{\equiv}CCH_3$, and 2 H_2 can be conducted in catalytic steady-state to > 40 turnover numbers on chiral and achiral single crystal surfaces (Figure 2). Remarkably this reaction can run without apparent deactivation of the Cu surface. Decomposition of tartaric acid (TA, $HO_2CCH(OH)CH(OH)CO_2H$) and aspartic acid on Cu surfaces occurs via a vacancy-mediated surface explosion mechanism with non-linear kinetics; $r = k_i\theta + k_e\theta(1-\theta)^2$, where θ is the adsorbate coverage and $(1-\theta)$ is the vacancy coverage. The rate constants parametrize an initiation step, k_i, and an explosion step, k_e. During temperature-programmed reaction experiments on naturally chiral Cu(*hkl*)$^{R\&S}$ surfaces these kinetics, coupled with the chirality of the adsorbates, lead to highly enantiospecific decomposition rates. Recently, Gellman has demonstrated that in the presence of a thermal molecular beam with a constant Asp flux, F_{Asp}, the decomposition of Asp on Cu(111) occurs catalytically and at steady-state to turnover numbers >40 without contamination or deactivation of the surface. Moreover, the decomposition rates at a given (T, F_{Asp}) manifest the two different steady-states predicted by the non-linearity of the decomposition kinetics. The unusual ability to catalytically decompose Asp on Cu, coupled with the ability to distinguish between *D*- and ^{13}C-*L*-Asp using mass spectrometry, opens an avenue for the future study of enantioselective catalysis on Cu(*hkl*)$^{R\&S}$ surfaces.

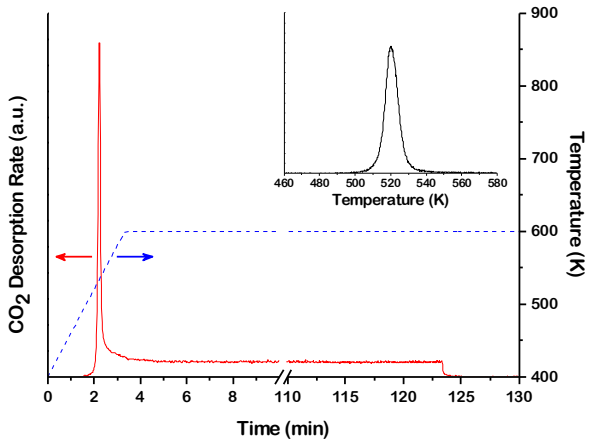

Figure 2: CO_2 desorption rates versus time during *D*-Asp decomposition on Cu(111). The clean surface at 400 K was initially saturated with *D*-Asp. In the presence of a constant flux of F_{Asp} = 0.53 ML/min, the sample was heated from 400 K to 600 K at 1 K/s and then held at 600 K for 2 hrs. The narrow CO_2 desorption peak at 2.2 min arises from explosive decomposition of adsorbed *D*-Asp and its area represents the CO_2 yield from one monolayer of *D*-Asp. The system then settles into a steady-state, constant CO_2 desorption rate with the surface at 600 K until the shutter is closed after 123 min. The integrated area under the steady-state CO_2 desorption signal corresponds to the decomposition of ~40 ML of *D*-Asp. The turnover number of >>1 demonstrates catalytic decomposition of *D*-Asp on Cu(111) (inset). The CO_2 TPR spectrum in the absence of a flux of *D*-Asp from decomposition of *D*-Asp at saturation coverage on Cu(111) while heating the surface at 1 K/s.

2.2 Chirally Templated Surfaces

Chiral Self-Assembly of Surface-Bound Propene

The adsorption of chiral molecules on a surface can be influenced by the chirality of already adsorbed molecules; as in the case of propylene oxide on Pt(111) (Zaera, 2013). Nonchiral adsorbates can exhibit surface-bound chirality when adsorbed on surfaces. When nonchiral propylene is adsorbed on Pt(111), the enantioselective adsorption of propylene oxide is amplified (Zaera, 2015). How the propylene molecules adsorb, their surface-bound chirality, and ability to self-assemble effects this enantioselective process is unknown. Further studies involving the direct observation of propylene on metal surfaces are necessary. Sykes probed the model system of propene on Cu(111). When propylene is deposited on Cu(111), annealed up to 40 K, and imaged by STM at 5 K, it is found that individually rotating molecules of both surface bound orientations are present at low coverages which coalesce into long range ordered domains. In Figure 3 (a), the *S* surface-bound orientation of propylene is highlighted by the translucent red triangles, the other *R* surface-bound orientation is the remaining three individual molecules. The chirality of the propylene molecules is not evident in the large domains. The domains themselves do not exhibit chirality, but the long-range order seen for such a small molecule is impressive, Figure 3 (b).

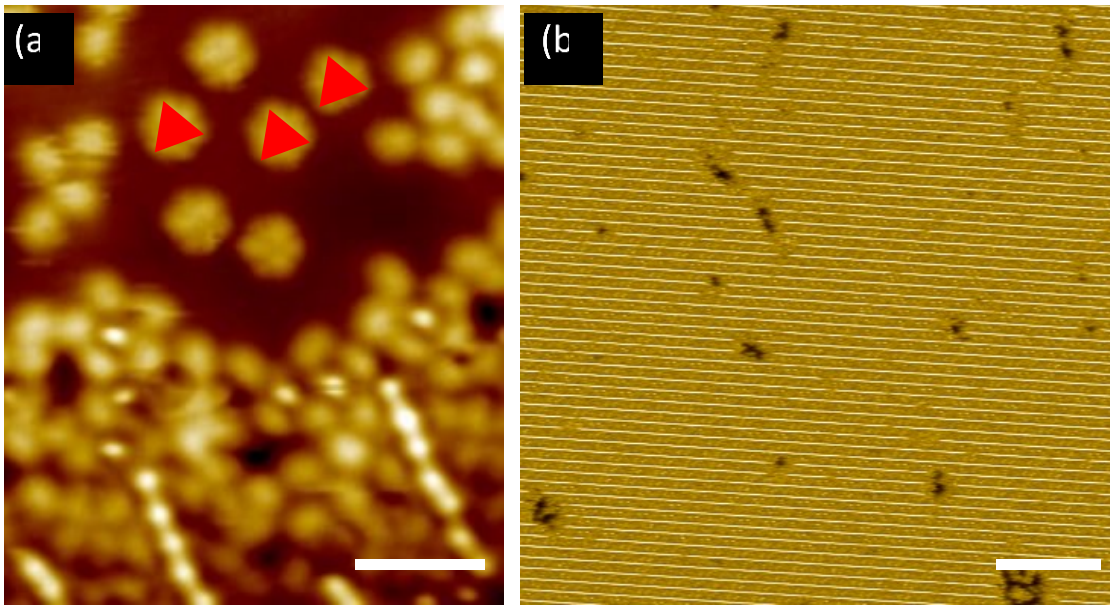

Figure 3: (a) Individually rotating propylene molecules can be seen at the edge of a domain. The red triangles highlight *S* surface-bound chirality of individual propylene molecules. 1.5 nm scale bar. (b) The long-striped propylene domains are hundreds of nanometers in size on Cu(111). 20 nm scale bar. The bright lines seen in the bottom of (a) are in a rotationally equivalent direction to those seen in (b) based on the underlying surface structure. The dark depressions seen in (b) are defects in the domain; areas of less propylene molecules.

Chirality in the growth of 2D Water layers

Water has an incredible ability to form a rich variety of structures, with e.g. 16 bulk ice phases identified as well as numerous distinct structures for water at interfaces or under confinement. Many of these structures are built from hexagonal motifs of water molecules and, indeed, for water on metal surfaces individual hexamers of just six water molecules have been observed. Here Sykes reports the results of low-temperature STM experiments and density functional theory (DFT) calculations which reveal a host of new structures for water-ice nanoclusters when adsorbed on an atomically flat Cu surface.

An example of the interesting new chiral structures found is the trilobed structure shown in Figure 4 (a). The STM image of this structure resembles a previously reported nine-water molecule trilobe structure, however, further experimental measurements reveal major features indicating that these complexes are larger than the previously reported nonamer. The first observation by Sykes is that there are two different types of trilobed features that exist in "up" and "down" orientations, resulting in four structures instead of the two expected for the water nonamer. This suggests that the rotational orientations for these trilobed features are due to actual rotations of the structure relative to the close-packed direction of the Cu(111) lattice and not the migration of monomeric units of water, as predicted and observed for the smaller water nonamers. The second observation is that the rotations of the trilobed structures are aligned almost parallel to the high-symmetry axis of the underlying surface and not with the $\sqrt{3}$ direction as predicted and observed for the water nonamer. Experimental measurements indicate that one type of trilobe structure is rotated +4° from the close-packed direction of the Cu(111) surface whereas the second is orientated −4°, making these structures chiral.

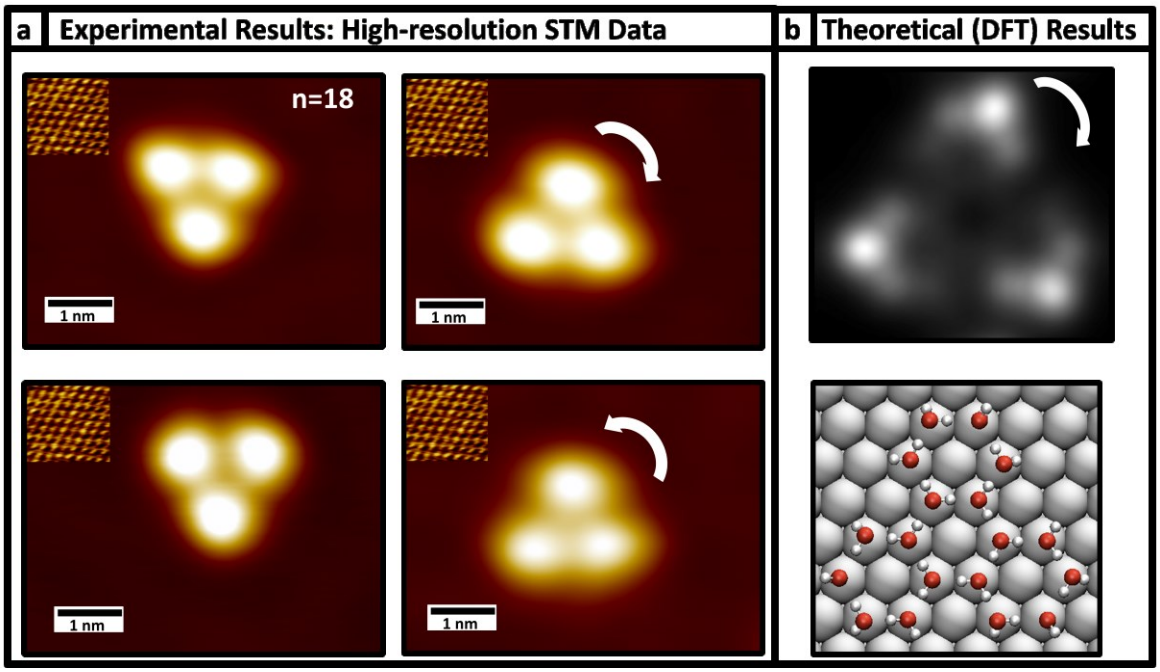

Figure 4: (a) High-resolution STM images acquired at 5 K of two chiral tri-lobed structures, with each chiral conformer found in an "up" and "down" orientation. The lobe-lobe distances are larger than predicted distances for the water heptamer. (b) (top) A DFT-simulated image of the proposed tri-lobed structure, indicating that the three double acceptor (DA) water molecules image as 3 bright protrusions. Since the positions of DA molecules can alternate within their respective hexamer rings, tri-lobed clusters image as chiral structures. (bottom) DFT-calculated structure proposed for the tri-lobed structures, which consist of four hydrogen-bonded hexamers, or of 18 water molecules.

Density functional theory (DFT) calculations by Sykes predict that the most stable cluster for this trilobed structure (with $E_{ads} = -650$ meV) is composed of four H-bonded hexamers, or 18 water molecules ($n = 18$), with three buckled hexamers arranged around a flat central water hexamer (Fig. 4 (b)). This hexagonal arrangement is analogous to the organic compound triphenylene ($C_{18}H_{12}$). The DFT-calculated structure in Fig. 4 (b) shows that all water molecules sit on preferred atop sites, and each outer hexagonal ring contains one double acceptor (DA) water molecule. As with all the other proposed structures, DFT calculations show that the O–Cu distance in the DA molecules is ~3.20 Å, whereas the O atoms in the central flat hexamer lie much closer to the surface with O–Cu distances of ~2.20 Å. The three bright lobes observed in the STM images and the lack of resolution of the central flat hexamer are consistent with this structural prediction. Furthermore, the highest-lying molecules, the DAs, can iso-energetically H-bond in two different positions at the periphery of their respective buckled hexamer, giving rise to conformational isomers of the structure. Experimentally, this is confirmed by observations of chiral trilobed structures.

Structure of Amino Acid Chiral Templates

Tysoe has proposed that alanine on Pd(111) forms chiral tetramers in which the pocket at the center of the tetramer forms an enantioselective adsorption site. However, the structure was inferred from STM images of the tetrameric units, combined with DFT simulations. In order to test the proposed structures, Tysoe collected intensity-versus-voltage (I/V) curves of the low-energy electron

diffraction (LEED) patterns of alanine on Pd(111). Since alanine adsorbed on Pd(111) is extremely susceptible to electron-beam damage, LEED measurements were made using a current of ~500 fA using a pulse-counting delay-line LEED detector (DLD-LEED) system. This uses a low-current electron gun, microchannel plates for charge amplification, and delay line anode planes for signal detection, thereby minimizing electron-beam-induced damage. Because of the dead zone on the detector, some beams were missing in the LEED pattern. To allow all beams to be detected, the detector was rotated, and data were recorded at detector orientations of 267.5, 290, 312.5 and 335°. The results were then averaged over equivalent beams and detector orientations to minimize errors. No additional diffraction spots were found at any alanine coverage and only an increase in the background intensity was observed, confirming the absence of any long-range order on the surface. Since no long-range order is found following alanine adsorption on Pd(111), the adsorbate structure is determined from the substrate diffraction spots. The I-V data were analyzed using the CLEED: Automated Surface Structure package for an initial input structure from previous DFT calculations of the alanine zwitterion-anion dimer, the best fit structure yielded a satisfactory Pendry R-factor of 0.249, thus confirmed the correctness of the originally proposed structure. Such anionic-zwitterionic dimers are a class of hydrogen-bonding intermolecular interactions in proteins that are dominated by direct electrostatic interactions, in particular for residues such a lysine and arginine, known as salt bridges. While such salt bridges interactions are relatively weak in biological systems, the attractive interaction energy between the anion and the zwitterion in the dimer on Pd(111) in vacuo is found to be ~95 kJ/mol. It is proposed that the weakening in biological systems occurs because the electrostatic screening in biological (aqueous) media weakens the electrostatic interaction between the anion and zwitterion, causing their structures to relax to further weaken the anion-zwitterion interaction.

2.3 One-to-One Modifiers

Several reviews and perspective incorporating knowledge from Zaera's chiral work funded by this grant were published. An article by Zaera in *Top. Catal.* was an overview was provided of our work on the characterization of chiral modifiers for the bestowing of enantioselectivity to metal-based hydrogenation catalysts, with specific reference to the so-called Orito reaction. We started with a brief discussion of the use of infrared absorption spectroscopy (IR) for the characterization of chemical species at liquid–solid interfaces, describing the options available as well as the information that can be extracted from such experiments and the advantages and disadvantages associated with the technique. Zaera then summarized the main results that we have reported to date from our IR study of the adsorption of cinchona alkaloids and related compounds from solutions onto platinum surfaces. Several observations were highlighted and placed in context in terms of the existing knowledge and their relevance to catalysis. Key conclusions include the uniqueness of the nature of the adsorbed species when in the presence of the solvent (versus when the uptake is done under vacuum, or versus the pure or dissolved molecules), the fact that each modifier adopts unique and distinct adsorption geometries on the surface and that those change with the concentration of the solution in ways that correlate well with the performance of the catalyst, the potential tendency of at least some of these chiral modifiers to bind to the surface primarily via the nitrogen atom of the amine group, not the aromatic ring as it is often assumed, and the observation that the ability of one modifier to dominate the catalytic chemistry in solutions containing mixtures of two or more of those is linked to their capacity for displacing each other

from the surface, which in turn is determined by a balance between the strength of their binding to the surface and their solubility in the liquid solvent.

A general review on chiral adsorption on solid surfaces published by Zaera in *Chem. Soc. Rev.* surveyed the main advances made in recent years on the understanding of chemical chirality at solid surfaces. We started with a description of surface chirality and of the different ways that chirality can be bestowed on solid surfaces, and then expanded on the studies carried out to date to understand the adsorption of chiral compounds at a molecular level. Zaera summarized the work published on the adsorption of pure enantiomers, of enantiomeric mixtures, and of prochiral molecules on chiral and achiral model surfaces, especially on well-defined metal single crystals but also on other flat substrates such as highly ordered pyrolytic graphite. Several phenomena were identified, including surface reconstruction and chiral imprinting upon adsorption of chiral agents, and the enhancement or suppression of enantioselectivity seen in some cases upon adsorption of enantiomixtures of chiral compounds. The possibility of enhancing the enantiopurity of adsorbed layers upon the addition of chiral seeds and the so-called "sergeants and soldiers" phenomenon were presented. Examples were provided where the chiral behavior has been associated with either thermodynamic or kinetic driving forces. Two main approaches to the creation of enantioselective surface sites were discussed, namely, via the formation of supramolecular chiral ensembles made out of small chiral adsorbates, and by adsorption of more complex chiral molecules capable of providing suitable chiral environments for reactants by themselves, via the formation of individual adsorbate:modifier adducts on the surface. Finally, a discussion was offered on the additional effects generated by the presence of the liquid phase often required in practical applications such as enantioselective crystallization, chiral chromatography, and enantioselective catalysis.

2.4 Catalytic Studies

Several synthetic strategies were developed by Zaera for the preparation of chiral dendrimer-encapsulated Pt nanoparticle (Pt DEN) catalysts. In one approach, regular OH-terminated polyamidoamine (PAMAM) dendrimers were first derivatized with cinchonidine using “click” chemistry and sebacic acid as a linker. As many as half of the 64 terminal OH groups in a 4th generation PAMAM dendrimer could be modified this way, and the overall cinchonidine content could be tuned by controlling the CD:PAMAM ratio during synthesis. Platinum nanoparticles were then added to these cinchonidine-modified dendrimers. In an alternative route, regular Pt DENs were made first using PAMAM, and the resulting material was then derivatized with cinchonidine. The two synthetic routes proved successful, but led to materials with different spectroscopic and catalytic properties, presumably because the metal nanoparticles in the first case are made near the cinchonidine functionality, in the outside of the dendrimer structure rather than in its inside, as believed to be the case with the second procedure. A potential complication related to the poisoning of the Pt nanoparticle surface during synthesis was also identified in the second protocol. The performance of these catalysts for the hydrogenation of α-ketoesters proved to be poor in all cases, presumably because of a number of problems associated with mass transport limitations inside the dendrimer structures and restricted flexibility of the outer chiral branches, which may not be able to interact with the catalytic surfaces. Nevertheless, interesting synthetic lessons were derived from our work with potential value for other applications.

In addition, in a first step toward designing multifunctional tandem catalyst capable of promoting chiral steps, a synthetic procedure was developed by Zaera to prepare dual acid–base catalysts on a single platform. Mesoporous SBA-15 was derivatized using known grafting chemistry via the following steps: (1) addition of Boc-protected 3-aminopropyltriethoxysilane; (2) controlled use of UV/ozonolysis to selectively remove the exterior groups; (3) decoration of the exterior sites freed in Step 2 with 3-mercaptopropyltriethoxysilane; (4) selective oxidation of the mercaptan groups to sulfonic acid; and (5) pyrolytic deprotection of the amine. The resulting catalysts contain sulfonic acid functionality on the external surfaces and entrance of the pores and amino groups deep inside those pores, at coverage ratios that can be controlled by tuning the exposure time during the UV/ozonolysis step. The samples were fully characterized by ^{29}Si and ^{13}C solid-state NMR, infrared absorption spectroscopy, acid–base titrations, and N_2 adsorption isotherms measurements, and they were successfully tested for the promotion of a cascade Henry reaction. Optimum performance was seen with the catalyst having an overall 1:2 acid:base molar ratio.

Catalytic reactions were also carried out by Tysoe on model single-crystal catalysts using a high-pressure reactor incorporated into a UHV chamber. Tysoe previously identified the stereodirecting interactions for a model system that mimics an effective heterogeneous chiral catalyst for the Orito reaction for the enantioselective hydrogenation of α-ketoesters. Here, Tysoe explored the interactions between methyl pyruvate and a cinchonidine mimic, naphthyl ethylamine (NEA) that can be conveniently introduced into UHV. This work showed that there was a preferential docking of the enol tautomer of methyl pyruvate to the NEA. This resulted in the formation of a more-easily hydrogenated carbon-carbon double bond as demonstrated by temperature-programmed desorption (TPD) experiments. This work also showed that the interaction between the prochiral methyl pyruvate was controlled by binding of the C=C double bond of the enol tautomer of methyl pyruvate and its ability form hydrogen bonds to the chiral ethylamine center, where the interaction energy between the methyl pyruvate and the NEA corrected with the length of the hydrogen bond. This observation is important because the enhanced reactivity of the enol form of methyl mitigates the influence of the less reactive keto form of methyl pyruvate on unmodified sites which will produce racemic products. Finally, the resulting methyl pyruvate could adsorb in either a pro-(*R*) or pro-(*S*) adsorption geometry, where the ratio of the geometries depends on temperature because of the different binding strengths of the various geometries. Tysoe postulated that the enantioselective excess (*ee*) of the products in an enantioselective hydrogenation reaction on Pd(111) should correlate with the relative coverages of the pro-(*R*) and pro-(*S*) structures. In order to test this postulate, Tysoe modified a UHV system that contains an integral high-pressure reactor cell to be able to carry out high-pressure catalytic reaction under realistic conditions of to measure the *ee* of methyl pyruvate hydrogenation on NEA-modified Pd(111) surfaces. The system was equipped with a Knudsen source for modifying the surface with NEA and a quadrupole mass spectrometer for measuring the CO desorption yield in order to conveniently gauge the NEA coverage by CO blocking. The gases are mixed in this system using an external loop with a recirculating pump to ensure that the reacting gases are well mixed and attached to gas-chromatograph (GC) for sample analysis. A septum was also included in the recirculating loop to enable samples to be extracted for subsequent analysis in a GC-MS system in order to identify the nature of the reaction products and to calibrate the retentions times of the GC. However, during meetings with the Program Managers Drs. Chris Bradley and Viviane Schwartz at the Catalysis Science program of the Chemical Sciences, Geosciences and Biosciences Division of Basis Energy Science at DOE indicated that the focus on enantioselectivity did not fit into the energy mission

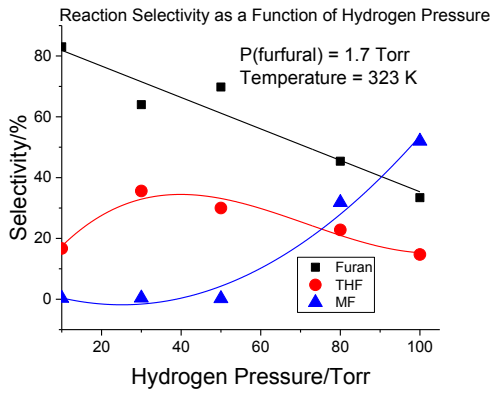

Figure 5: Selectivity to furan, tetrahydrofuran (THF)and methyl furan(MF) formation as a function of hydrogen pressure for reaction of 1.7 Torr of furfural at 323 K catalyzed by clean Pd(111).

of DOE. Following consultation with the Program Managers, it was agreed that the direction of the program should be modified to address the issue of using organic selectivity modifiers, analogous to those being used to influence enantioselectivity, as modifiers for reactions related to biofuel production. Accordingly, we studied the hydrogenation of furfural on a Pd(111) model catalyst. To supplement this work, and to provide a basis for understanding the surface chemistry reactions at high pressures, Tysoe measured the reflection-absorption infrared spectra (RAIRS) of furfural and related molecules (furan, methyl furan and furfural alcohol) on Pd(111).

Reactions were carried out using a Pd(111) single crystal model catalyst that was cleaned in UHV and transferred directly to the high-pressure reaction cell using a constant furfural pressure of 1.7 Torr, while the reaction temperature and hydrogen pressure were varied. Background experiments were carried out for a carbon-covered Pd(111) sample to confirm that the reaction was catalyzed by the Pd(111) single crystal. The reaction products were analyzed using a gas chromatograph (GC) by analyzing aliquots of the reaction mixture as a function of time.

The major products detected during the reaction were tetrahydrofuran (THF), furan and methyl furan (MF). No furfuryl alcohol was detected. The selectivity to these reaction products is shown in Figure 5 for furan (■), THF (●) and MF (▲), where the lines are included as a guide to the eye. The selectivity appears to be controlled by the rates at which furfural decarbonylates to form furyl species compared to the rate at which furfural hydrogenates to form

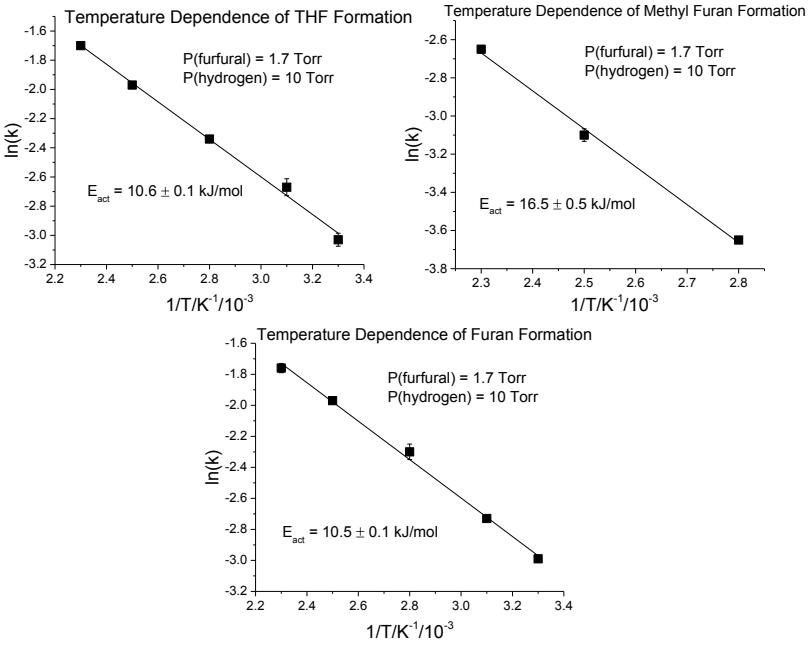

Figure 6: Arrhenius plots for the formation of tetrahydrofuran, methyl furan and furan formation using a pressure of 1.7 Torr of furfural with 10 Torr of hydrogen.

methyl furan. At low hydrogen pressures, the reaction is dominated by decarbonylation to form mostly furan. More tetrahydrofuran is formed at higher hydrogen pressures, while as the hydrogen

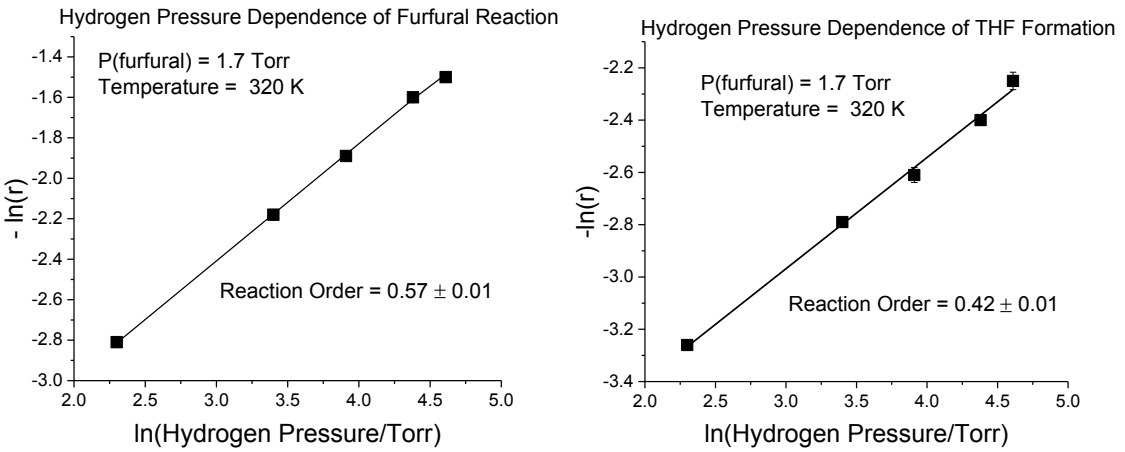

Figure 7: The hydrogen pressure dependence of the rate of furfural removal and the rare of tetrahydrofuran formation at 323 K with a furfural pressure of 1.7 Torr.

pressure increases to above ~70 Torr, hydrogenation of furfural to methyl furan becomes significant.

Arrhenius plots for the formation of the major reaction products are displayed in Figure 6. The activation energies for furan and tetrahydrofuran are very similar (~10.5 kJ/mol) suggesting that the rate-limiting steps for their formation are identical, presumably corresponding to decarbonylation of the furfural. The activation energy for methyl furan formation is somewhat higher (~16.5 kJ/mol) and corresponds to the energy barrier for the rate-limiting step of furfural hydrogenation.

The hydrogen pressure dependence for the removal of furfural at 323 K is shown in Figure 7, the overall reaction rate is approximately ½ order in hydrogen pressure. The dissociative adsorption of H_2 varies as $\sqrt{P(H_2)}$ and indicates that the rate-limiting step is controlled by the addition of a single hydrogen. This is confirmed by the hydrogen pressure dependence of the rate of tetrahydrofuran formation (Figure 7), which also show an approximately half-order dependence in hydrogen pressure. The overall kinetics are therefore controlled by the relative rates of decarbonylation of furfural to

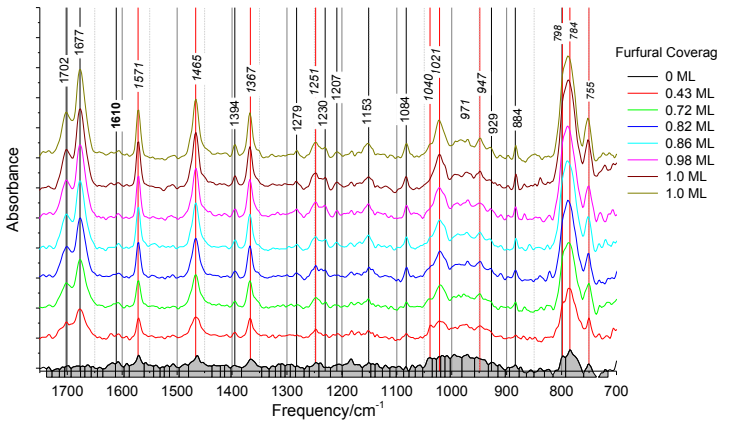

Figure 8: Infrared spectra of low coverages of furfural adsorbed on Pd(111) at ~90 K as a function of furfural coverage, where the coverages are indicated in the figure.

form furyl groups compared to the rate of hydrogenation of furfural to form methyl furan. Note that no furfural alcohol is found under the reaction conditions.

Reflection-absorption infrared spectra (RAIRS) were collected for furfural on clean and hydrogen-covered Pd(111) as a function of temperature and dosing conditions to provide insights into the high-pressure reaction mechanisms

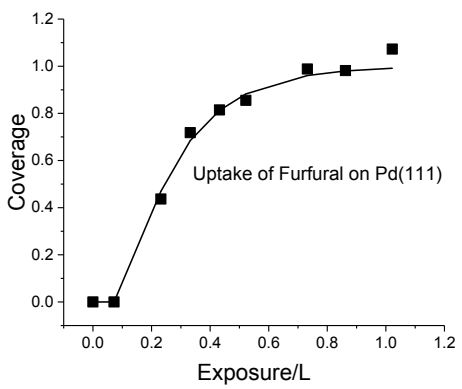

Figure 9: Uptake for furfural on Pd(111) at low temperatures from the variation in the integrated intensity of the carbonyl stretching modes as a function of exposure.

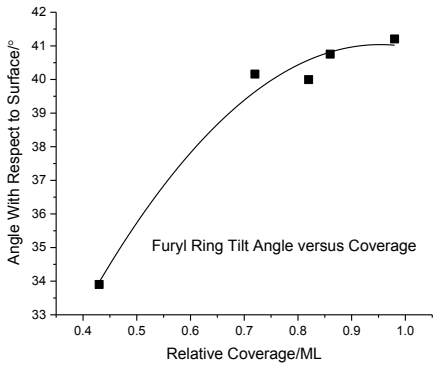

Figure 10: Plot of furfural tilt angle with respect to the surface as a function of the relative coverage of furfural adsorbed on Pd(111) at ~90 K.

Tysoe first explored the structure of furfural on Pd(111) at low temperatures, where the conformation of the aldehyde group and the molecular tilt angle can change. The infrared results (Figure 8) show two distinct regimes as a function of exposure at 90 K. At low coverages, when the spectra shows no intensity at ~1707/1677 cm^{-1}, assigned to the carbonyl stretching region, suggests that the CHO group lies flat on the surface. Higher coverages cause the carbonyl modes to appear suggesting that the furfural adopts a more tilted geometry and the vibrational frequencies are close to those found for the liquid furfural, indicating that furfural adsorbs molecularly.

Uptake into the high-coverage, tilted state is gauged from the variation in the intensity of the carbonyl stretching modes with exposure and the results are displayed in Figure 9. The spectra in Fig. 8 also shows modes at 1702 and 1677 cm^{-1} indicating the presence of both the *cis* and *trans* conformers of furfural following adsorption at ~90 K. Measuring the ratios of the intensities of the 1702 and 1677 cm^{-1} CHO modes as a function of exposure reveals that the intensity ratio is independent of the furfural coverage and the relative coverage and shows that 40% of the furfural exists as the trans conformer and 60% as the cis conformer. The variation in tilt angle with coverage is calculated from the variation in intensity of an A' (at 1465 cm^{-1}) and A" (784 cm^{-1}) symmetries as a function of coverage. The results are displayed in Figure 10, which shows that the furfural tilt angle varies from ~35º with respect to the surface at a relative coverage of ~0.4 ML to ~41º as the coverage approaches saturation. This result is on accord with DFT calculations by Vlachos.

The effect of heating on the vibrational spectra for a monolayer of furfural adsorbed on Pd(111) at ~90 K is shown in Figure 11. The spectra were obtained by heating that sample to the indicated

temperature for ~5 s and then allowing the sample to cool once again to ~90 K, following which the spectra were recorded. The vibrational frequencies for annealing temperatures below ~125 K are essentially identical to those found in Fig. 8. However, changes are noted in the ratios of the intensities of the C=O stretching modes at ~1702 and 1677 cm^{-1}, indicating a change in the cis-to-trans ratio of furfural. This is accompanied by a decrease in intensity of the furfural vibrational modes and the appearance of a broad features at ~1620 cm^{-1}. In addition, shifts are seen in the 1465 cm^{-1} mode to 1474 cm^{-1}, of the mode at 1248 to 1282 cm^{-1}. The remaining mode at ~784 cm^{-1} is due to some remaining cis-furfural on the surface, and an additional mode appears at ~761 cm^{-1}. The feature at ~1616 cm^{-1} is a due to a carbonyl stretching mode and is consistent with the onset of decarboxylation, suggested by DFT calculations to be due to the dehydrogenation of the CO group, where DFT calculations indicate that the activation barrier for this process is ~ 1eV (~95 kJ/mol). The variation in the carbonyl modes intensities is summarized in Figure 12 as a function of annealing temperature. Additional modes are detected at 1730 cm^{-1} at ~250 K and higher, and appear at frequencies lower than would be expected for CO adsorbed on Pd(111). In order to establish the origin of the peaks in this region, the adsorption of furan was studied on clean Pd(111) and the results are displayed in Figure 13. This shows vibrational frequencies following furan adsorption at low temperatures that agree with gas-phase furan and the relative intensities of the vibrational modes indicate that furan is tilted on the surface as found in previous work. This shows a mode at ~1730 cm^{-1} due to furan decomposition thus conforming the assignment made above. A similar vibrational frequency was detected following methyl furan adsorption on Pd(111) on heating to ~225 K (data not shown).

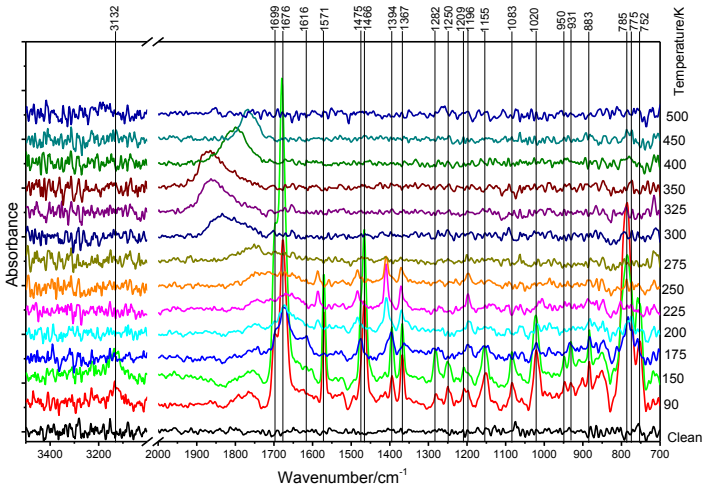

Figure 11: Infrared spectra of furfural adsorbed on Pd(111) at ~90 K as a function of annealing temperature, where the annealing temperatures are indicated adjacent to the corresponding spectrum.

The overall reaction pathway of furfural on Pd(111) is in accord with the high-pressure reactions of Pd(111) described above in which adsorbed furfural decarbonylates to produce a furyl intermediate which, in the high-pressure experiments, hydrogenates to furan and tetrahydrofuran.

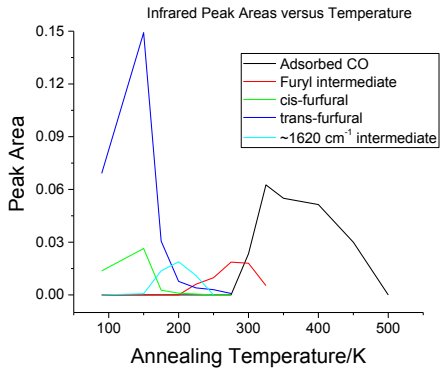

Figure 12: Variation in the integrated intensities of the vibrational modes in the carbonyl stretching region.

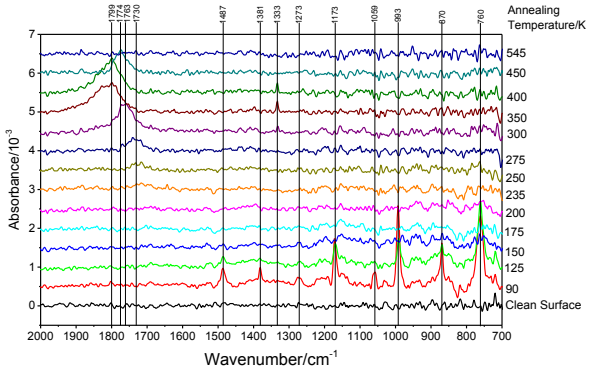

Figure 13: Infrared spectra of furan adsorbed on Pd(111) at ~90 K as a function of annealing temperature, where the annealing temperatures are indicated adjacent to the corresponding spectrum.